Cite this article: Hur, O., Tutika, R., Klemba, N., Markvicka, E.J. and Bartlett, M.D., "Designing liquid metal microstructures through directed material extrusion additive manufacturing." Additive Manufacturing 79 (2024): 103925.

This version of the article has been accepted for publication, access the version of record at:

https://www.sciencedirect.com/science/article/pii/S2214860423005389

Designing liquid metal microstructures through directed material extrusion additive manufacturing

Ohnyoung Hur[1†], Ravi Tutika[1,2,†], Neal Klemba[3], Eric J. Markvicka[4,5,6*], and Michael D. Bartlett[1,2*]

[1]Mechanical Engineering, Soft Materials and Structures Lab, Virginia Tech, Blacksburg, VA 24061, USA.
[2]Macromolecules Innovation Institute, Virginia Tech, Blacksburg, VA 24061, USA.
[3]Mechanical Engineering, Brown University, Providence, RI 02912, USA.
[4]Mechanical & Materials Engineering, Smart Materials & Robotics Lab, University of Nebraska–Lincoln, Lincoln, NE 68588
[5]Electrical & Computer Engineering, University of Nebraska–Lincoln, Lincoln, NE 68588
[6]School of Computing, University of Nebraska–Lincoln, Lincoln, NE 68588

[†]equal contribution
[*]To whom correspondence should be addressed: eric.markvicka@unl.edu, mbartlett@vt.edu

Abstract

Material extrusion (MEX) of soft, multifunctional composites consisting of liquid metal (LM) droplets can enable highly tailored properties for a range of applications from soft robotics to stretchable electronics. However, an understanding of how LM ink rheology and print process parameters can reconfigure LM droplet shape during MEX processing for in-situ control of properties and function is currently limited. Herein, the material (ink viscosity, and LM droplet size) and process (nozzle velocity, height from print bed, and extrusion rate) parameters are determined which control LM microstructure during MEX of these composites. The interplay and interdependence of these parameters is evaluated and nearly spherical LM droplets are transformed into highly elongated ellipsoidal shapes with an average aspect ratio of 12.4 by systematically tuning each individual parameter. Material and process relationships are established for the LM ink which show that an ink viscosity threshold should be fulfilled to program the LM microstructure from spherical to an ellipsoidal shape during MEX. Additionally, the thin oxide layer on the LM droplets is found to play a unique and critical role in the reconfiguration and retention of droplet shape. Finally, two quantitative design maps based on material and process parameters are presented to guide MEX additive manufacturing strategies for tuning liquid droplet architecture in LM-polymer inks. The insights gained from this study enable informed design of materials and manufacturing to control microstructure of emerging multifunctional soft composites.

Keywords: Direct ink writing, liquid metal, additive manufacturing, microstructure, rheology

1 Introduction

Soft, multifunctional polymer composites are essential for fields ranging from soft robotics to physical intelligence [1–5]. The properties of these functional composite materials are controlled by the material constituents and how these multi-phase systems are assembled and structured across a range of length scales. In the recent years, additive manufacturing (AM) of functional polymeric materials has rapidly progressed due to the versatility in materials choice combined with the in-situ programming capabilities [6–9]. This results in process-structure-property relationships that enable a unique combination of functional and mechanical characteristics [10–13]. The programmed materials developed using AM techniques have shown potential for achieving excellent thermal, electrical, and adaptive properties for next generation high performance multifunctional materials desirable for sensors, dielectrics, energy harvesters, and health monitoring applications and devices [14–20].

Direct ink writing (DIW) is an material extrusion AM technique that can enable versatile, novel material systems with a unique property and application space combined with the ease of design and rapid manufacturing for complex geometries [21–24]. DIW has been widely utilized to create films and structures using polymeric resins and has in turn enabled significant advancements in polymer composite printing due to the precise control of the orientation, loading, and location of the functional fillers within a printed part [25–28]. The functional and mechanical properties of a printed part in DIW are dictated by two groups of parameters - material/ink and printing/process [29, 30]. The former are related to the initial as-prepared properties of the ink such as polymer matrix viscosity, cross-linking type, filler shape, size, and phase (solid/liquid) [31]. Whereas the process parameters include the extrusion rate, printing speed, nozzle shape, nozzle size, nozzle height from print bed, the degrees of freedom for the nozzle, and the presence of any external fields (thermal, electrical, UV light, magnetic) [32, 33]. These two groups have interrelated and interdependent effects on the final characteristics of the part. Although, several rigid filler systems have been

demonstrated that can induce alignment in the filler, there is little knowledge of process-structure relationships in emerging systems that are based on liquid droplet fillers [34–37].

Liquid metal (LM) composites are attractive to a variety of technologies including soft robotics and wearable electronics owing to their soft mechanical compliance with high performance thermal, electrical, and mechanical properties [38–45]. One of the key enabling features of these functional properties is the unique liquid nature of the filler which allows droplet shape (i.e. aspect ratio), size, and connectivity to be tuned during processing and mechanical deformation. This has imparted advanced functional and mechanical properties to these soft composites. For example, the ability to tune aspect ratio from spherical to ellipsoidal shapes has resulted in over 70× enhancement in thermal conductivity by creating oriented and anisotropic thermal pathways [40, 46–48]. Reconfiguration of the insulated and isolated LM droplets to an electrically conductive and connected network through mechanical activation has produced unconventional strain-independent electrical conductivity and robust self-healing abilities [49–53]. Further, tunability in the droplet size and spatial arrangement has enhanced adhesion control [54–56] while orientated droplets have increased toughness and eliminated cracks [41, 57]. This prior work illustrates that LM microstructural aspects such as shape, size, connectivity, and spatial organization impart exceptional mechanical and functional behavior to these soft functional composites.

Previous research efforts have also shown that due to the liquid nature of the LM, DIW technology can be readily applied to create soft circuit traces through modifying the adhesion of LM inks [58], rheological modification with solid metal fillers [59], and multi-layered circuits with a LM layer followed by a silicone layer [60]. Hybrid approaches have also been employed to create deployable and reconfigurable multifunctional lattice materials [61]. There have also been approaches where LM emulsion inks are created as silicone oil greases [62] or LM-polymer emulsions [63] which have been either adapted or present a potential for DIW technologies. Recently, it has been demonstrated that the LM droplet shape and orientation can be controlled during DIW processing [64]. The on-demand morphology control

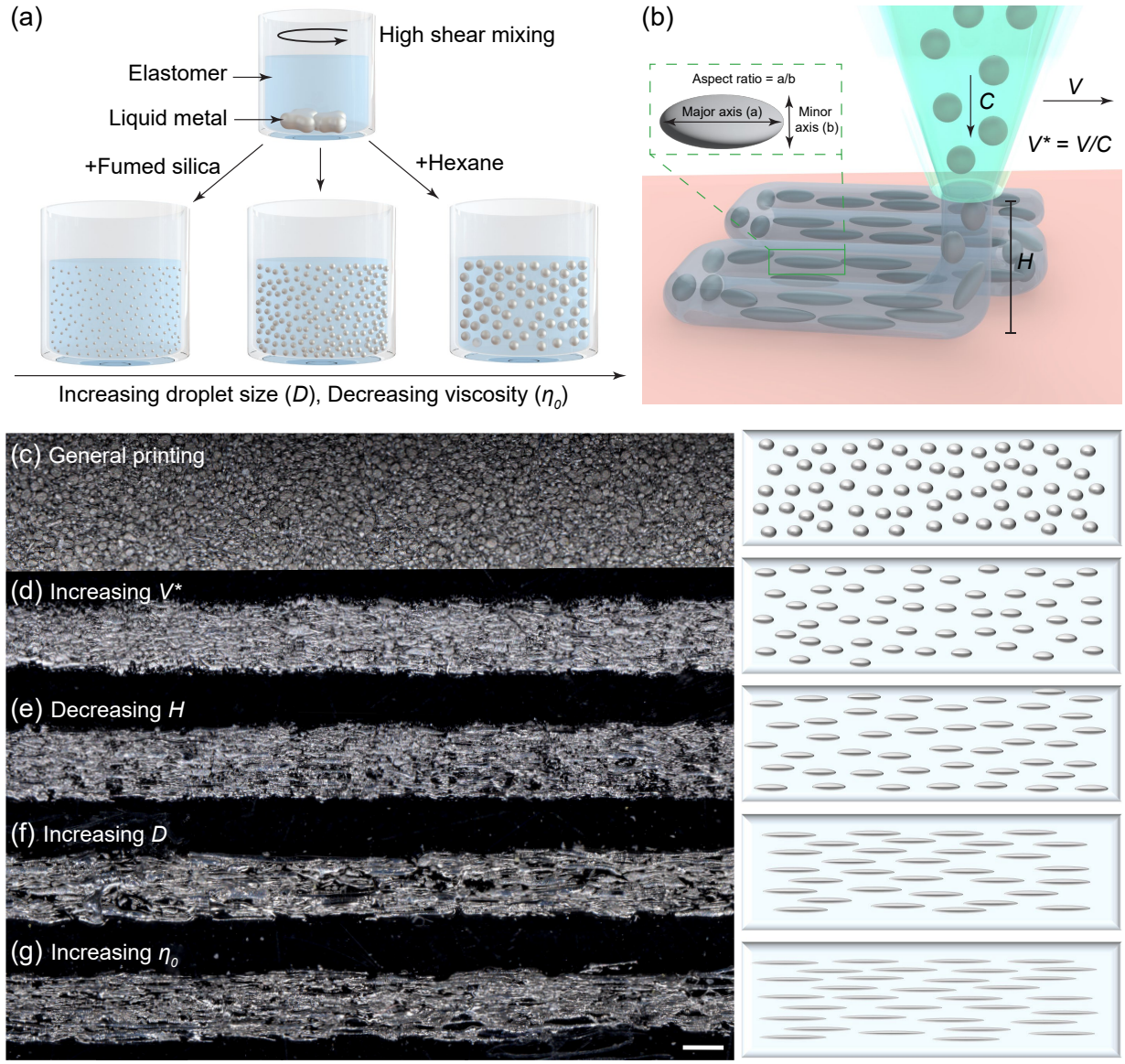

Fig. 1 Material and process parameters in DIW printing. (a) Ink and material parameters that are controlled by rheological modification. (b) Schematic showing the DIW printing parameters and resulting droplet aspect ratio. Optical microscopy and schematics illustrations showing the resulting microstructures in a variety of ink/printing conditions including, the (c) General condition, (d) Increasing V^*, (e) Decreasing H, (f) Increasing D, (g) Increasing η_0. Scale bar is 500 μm.

during DIW printing is intriguing because the morphology governs the material properties and performance of the composite. This enables the creation of parts with programmable material properties utilizing a single manufacturing system and ink. These capabilities can advance the utility of DIW systems for the fabrication of functional devices for applications in energy harvesting [19] and strain sensors [20] to morphing structures [24] and gripping devices [27]. However, the interdependence of ink properties and printing process parameters that is essential to tune final part microstructure requires further investigation.

Here, we determine how ink properties (Fig. 1(a)) and printing process parameters (Fig. 1(b)) control LM droplet microstructure programming during DIW. The functional emulsion ink contains nearly spherical LM droplets (Fig. 1(c)) that can be transformed into ellipsoidal shapes by increasing the nondimensionalized nozzle velocity ($V^* = V/C$, where V is the nozzle velocity and C is the extrusion velocity (C); Fig. 1(d)) or decreasing the nozzle height (H; Fig. 1(e)). This results in an increased average aspect ratio (AR) of elongated LM droplets from an initial AR of 1.3 to 3.7. Further, by increasing the droplet size (D; Fig. 1(f)) and zero-shear viscosity (η_0) of the LM ink (Fig. 1(g)), higher AR up to 12.4 can be achieved. Through these process and rheological relationships, we found that a viscosity threshold ($\eta_0 = 500$ Pa·s) should be fulfilled to tune the LM microstructure from spherical to ellipsoid shapes during DIW. Additionally, larger D plays a substantial role in achieving higher AR. In a series of experiments with glycerol and LM droplets, we further show the unique and critical role of the oxide layer on the LM droplets in retaining the AR of elongated LM droplets. We present these results in two quantitative design maps based on material and process parameters. These design maps are constructed to rationally guide the DIW printing of functional emulsion inks, enabling the precise control of liquid droplet architecture in soft composites.

2 Results and Discussion

2.1 Ink materials and composition

The LM inks used in this study are comprised of LM droplets at a volume ratio of $\phi = 50\,\%$ in PDMS and ExSil silicone elastomers. Fumed silica (FS) nanoparticles (lateral size: 16 nm) are added as a rheological modifier at two different weight ratios of $\psi = 5, 10\,\%$. The addition of FS to pristine elastomers or LM-elastomer inks resulted in an increase of η_0. Hexane (10 wt.% or 30 wt.%) was used as a solvent to decrease the viscosity and increase the droplet size (D) when required. A combination of LM, elastomer, FS, and hexane were used to study how different ink properties and printing process parameters can be utilized to control the aspect ratio of LM droplets in LM-polymer inks during DIW printing.

2.2 Effect of polymer matrix viscosity on LM droplet size

To investigate the effect of polymer viscosity on the D of LM droplets in LM inks, we performed rheological measurements and microscopic analysis on inks formulated with PDMS and ExSil elastomers. These two elastomers have an order of magnitude difference in viscosities as-purchased and we further modify their viscosity using FS nanoparticles. Fig. S1(a-b) shows that adding FS ($\psi = 5, 10\,\%$) to elastomers results in increased ink viscosity as FS restricts the flow of uncured elastomer [65, 66]. To obtain zero-shear viscosity (η_0), the Carreau-Yasuda model, which is developed for fitting rheological data of non-Newtonian fluids, can be defined by Equation 1:

$$\eta(\dot{\gamma}) = \eta_\infty + (\eta_0 - \eta_\infty)(1 + (\lambda\dot{\gamma})^\alpha)^{\frac{n-1}{\alpha}} \tag{1}$$

where η_∞: infinite shear viscosity, $\dot{\gamma}$: shear rate, λ: time constant, α: transition control factor, and n: power index [67–69]. As shown in Fig. 2(a) and Fig. S2(a), D of LM droplets

decreases as η_0 of the ink increases during LM-polymer ink formulation (see Material and Methods section for details). Fig. 2(b) and Fig. S2(b) also illustrate the difference in viscosity of the three inks by showing their spreading behavior on the substrate after being extruded from the DIW nozzle.

We consider two ink characteristics to evaluate its ability for LM microsturcture programming in our screw-based, mechanically driven DIW setup: (1) the rheological analysis indicates that the ink is shear thinning and (2) a sufficiently high η_0 (> 500 Pa·s) is obtained for tuning the shape of LM droplets in the printed ink [69,70]. We utilize η_0 obtained through the Carreau-Yasuda model to relate rheological properties to the elongation of LM droplets in Section 2.4. We hypothesize that in the LM-polymer inks with higher η_0, the uncured matrix induces significantly increased drag forces between the LM droplet and the matrix phase, which facilitates the elongation and retention of LM droplet shape in ellipsoidal state after being printed [71].

First, to evaluate the rheological properties of PDMS-based LM inks with different amounts of FS, steady-state flow shear rate sweep tests were performed. Fig. 2(c) shows that the addition of LM droplets to the PDMS prepolymer results in an increase in the overall viscosity of the ink. This behavior is expected and has been previously reported [35]. The viscosity of the LM-polymer inks can be further increased by increasing the loading of FS. All LM inks exhibit shear thinning behavior that is crucial for their ability to program LM microstructure in the DIW process, even as the viscosity is substantially increased.

For PDMS- and ExSil-based inks, the Carreau-Yasuda model provides a good fit for the data as presented in Fig. S3(a-b) and Table S1. From these fits, we obtain the η_0 value plotted in Fig. 2(d) for different PDMS-based LM inks, which is the viscosity of the system in the first Newtonian plateau region. The addition of LM droplets and FS to the ink increases η_0. The addition of LM to a high viscosity matrix results in smaller LM droplets as presented in Fig. 2(a) and (e). This is because when LM is mixed with a high viscosity resin by a shear mixer, it is subjected to a higher shear stress than a less viscous system [72,73]. Additionally,

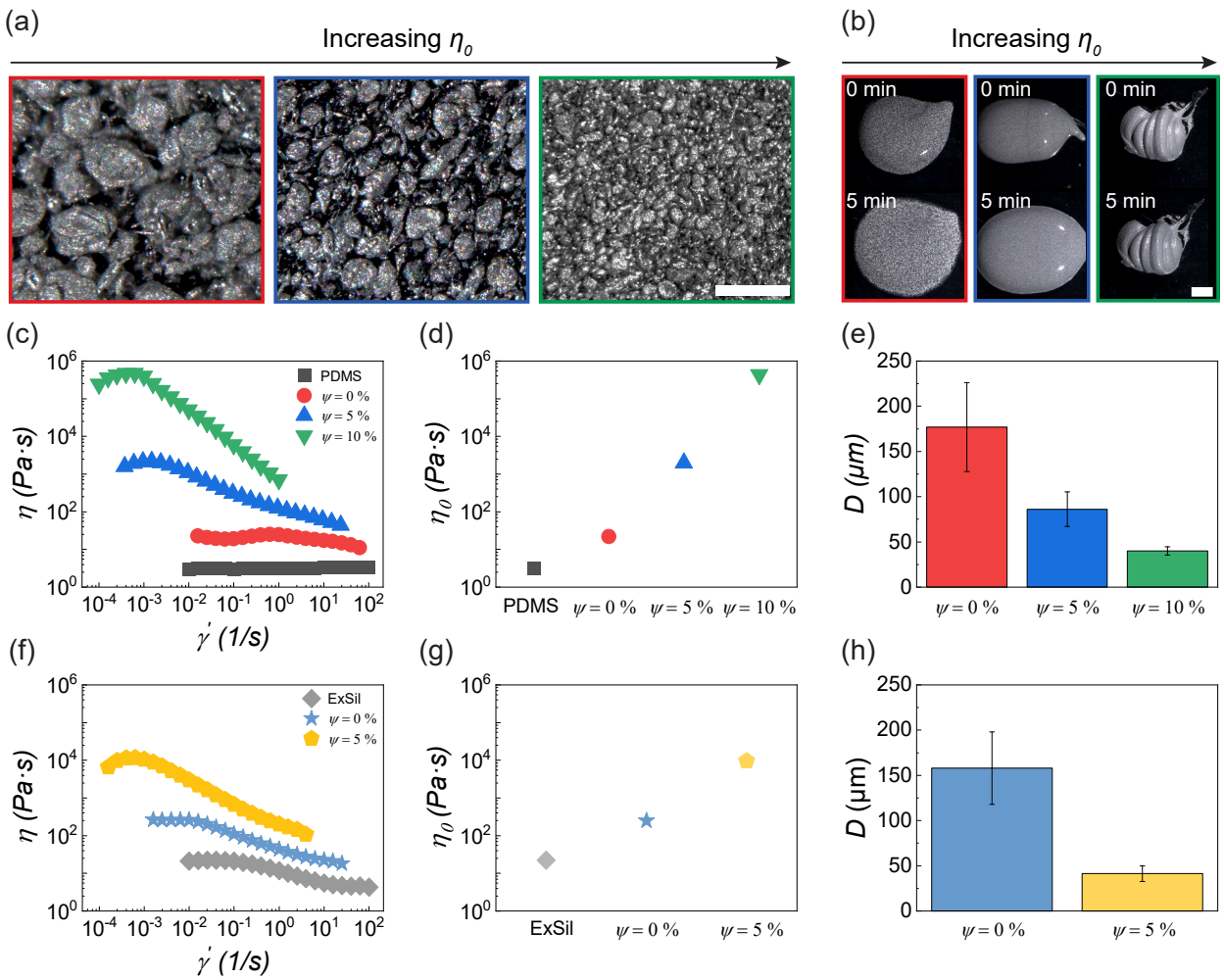

Fig. 2 Rheological analysis of different LM-polymer inks ($\phi = 50\,\%$) and viscosity effect on droplet size. Microscope images of PDMS-based LM inks: (a) The D of LM droplets decreases with increasing η_0. Scale bar is 200 μm. (b) Less spreading is observed after extrusion with increasing η_0. Scale bar is 2 mm. Colored borders for images in (a) and (b) indicate inks with similar colors in (c)-(e). (c) Apparent viscosity (η) vs. shear rate ($\dot{\gamma}$) of PDMS-based inks. ψ is the FS content in weight ratio. (d) Zero-shear viscosity (η_0) of different PDMS-based inks as measured from the Carreau-Yasuda model. (e) Droplet size (D) of LM droplets in different PDMS-based inks before printing. (f) η vs. $\dot{\gamma}$ of ExSil-based inks. (g) η_0 measured from the Carreau-Yasuda model of different ExSil-based inks. (h) D of LM droplets in different ExSil-based inks before printing. Error bars in (e) and (h) represent $\pm$ 1 standard deviation of log-normal fits to the particle analysis histograms from micrograph image analysis.

an ink with smaller LM droplets shows higher η_0 (Fig. S4). This is due to the higher surface-to-volume ratio in smaller LM droplets leading to an increase in the total droplet surface area in the system. The oxide layer on LM droplets strongly influences the rheological behavior

of LM [74], and as decreasing the droplet size for a given volume loading leads to higher surface area-to-volume ratio compared to larger droplets, the viscosity increases [75].

Our second set of rheological tests to study the effect of viscosity on D are performed on ExSil-based inks. As shown in Fig. 2(f), the addition of LM droplets results in an increased viscosity of the ink system and exhibit a shear-thinning behavior similar to the PDMS-based inks. When compared to PDMS-based inks, Fig. 2(g-h) also shows that ExSil-based ink results in an increases in η_0 and a decrease in D with the addition of FS. Therefore, we can conclude that the initial D of LM droplets is highly dependent on the viscosity of the polymer matrix for a given set of mixing conditions.

2.3 Effect of printing parameters (V^* and H) on AR

To investigate the factors that govern the shape control of LM droplets when printed, both PDMS- and ExSil-based inks were printed at different V^* (1, 6, and 12) and H (40, 150, and 300 μm) combinations. To tune V^* the nozzle velocity (V) is varied while the flow rate (C) of the ink during printing was held constant at 2.27 mm^3/s for all conditions. The AR of LM droplets for all samples was calculated from log-normal fits on the particle analysis histograms (Fig. S5-S9). As shown in Fig. 3(a-c), the AR of LM droplets in PDMS-based inks increased with increasing V^*, decreasing H, and increasing η_0 by increasing FS loading. For example, considering an LM ink consisting of PDMS with $\psi = 0\,\%$ and an average D of 177 μm. When printed with a $V^* = 1$ and $H = 300$ μm, the resulting LM droplets had an AR of 1.3. However, when the same ink is printed with different parameters, $V^* = 12$, $H = 40$ μm, the resulting droplets exhibit a higher AR of 2.0. Moreover, by introducing $\psi = 10\,\%$ to the PDMS ink with the same printing conditions, despite having a smaller D of 40.1 μm, the resulting droplets exhibited a significantly higher AR of 7.6. For this ink, the shape change of LM droplets as a function of different printing conditions is shown in Fig. 3(g). Furthermore, AR plateaus are observed in all samples with an increase in H.

To assess the influence of the shear stresses generated as the ink flows through the nozzle

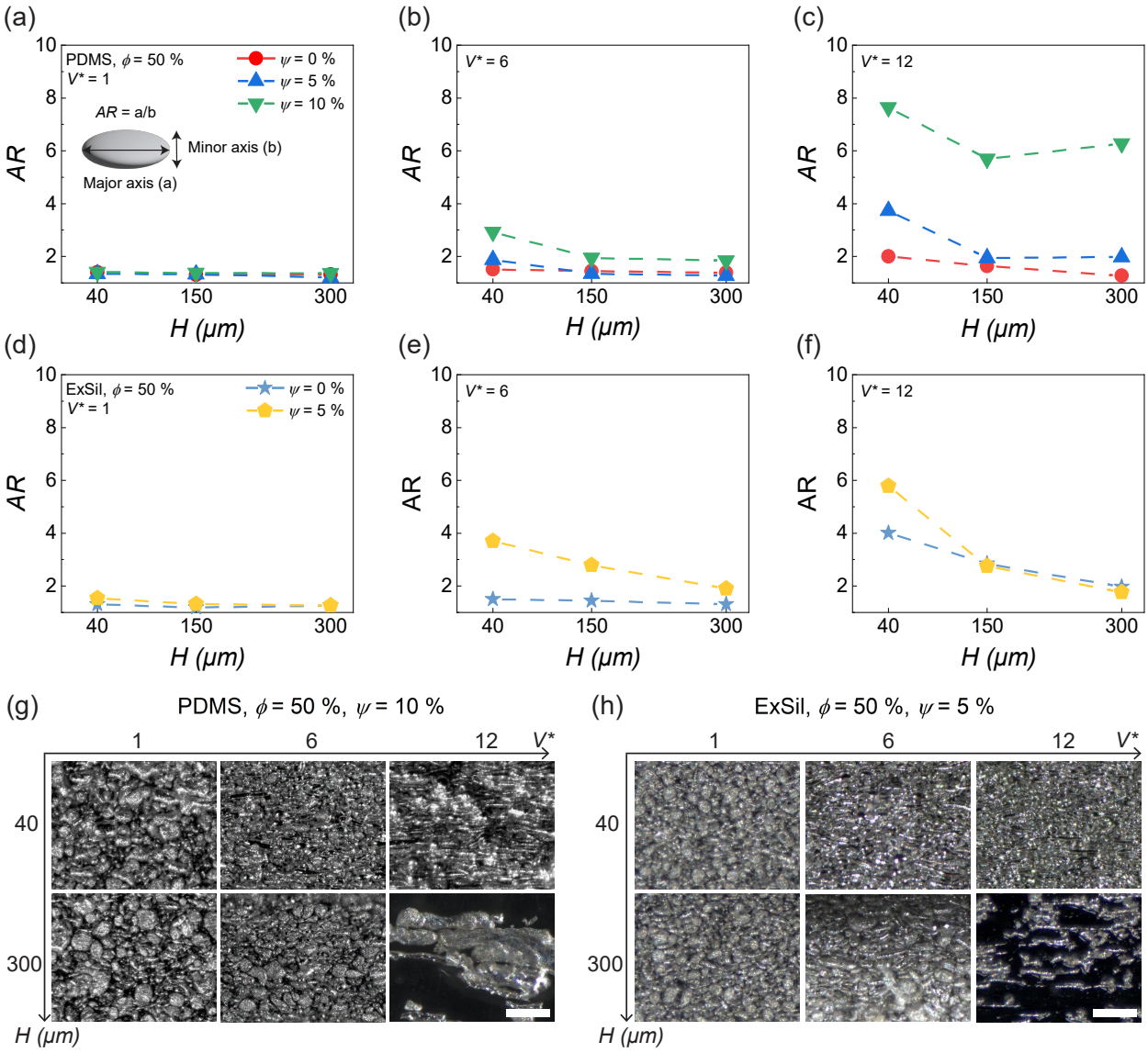

Fig. 3 LM droplet AR analysis in printed inks with varying rheological properties and printing conditions. The inset illustration in (a) describes how we define AR. Measured AR of LM droplets in PDMS-based inks with V^* = (a) 1, (b) 6, (c) 12. (b) and (c) follow the legend in (a). Measured AR of LM droplets in ExSil-based inks with V^* =(d) 1, (e) 6, (f) 12. (e) and (f) follow the legend in (d). Microscope images of printed inks with different V^* and H for (g) PDMS, $\psi = 10\,\%$, and (h) ExSil, $\psi = 5\,\%$. Scale bars are 100 μm.

on droplet shape, we conducted extrusion of PDMS-based ink without any movement of the print head. We observed no significant changes to the shape of LM droplets due to extrusion through the nozzle (Fig. S10). This result indicates that the resulting LM droplet shape is controlled by the shear generated between the nozzle and print bed ($\dot{\gamma}_{print\,bed} = V/H$), where

printing conditions with higher V^* and lower H produce a higher shear rate during printing, resulting in higher LM droplet AR. Shear rates ($\dot{\gamma}_{print\,bed}$) for different printing conditions are presented in Table S2. As shown in Fig. S11(a), higher shear rate results in higher shear stress on the printed material with increased η_0 (more FS content). Moreover, inks exhibit viscoelastic properties (Fig. S11(b)), when the shear stress is sufficiently high ($G^{'} < G^{''}$) the ink can flow by shearing. Therefore, at higher V^* and lower H printing condition, LM droplets are deformed by the rapid movement of the nozzle tip resulting in a higher AR.

Similar trends to the PDMS-based inks are observed in ExSil-based inks (Fig. 3(d-f)). The AR of LM droplets in ExSil-based inks increases from 1.3 ($\phi = 50\,\%$, $\psi = 0\,\%$, $V^* = 1$, $H = 300\ \mu m$) to 5.8 ($\phi = 50\,\%$, $\psi = 5\,\%$, $V^* = 12$, $H = 40\ \mu m$). ExSil-based ink ($\phi = 50\,\%$, $\psi = 5\,\%$) also shows large LM droplet shape change that depends on the printing conditions as shown in Fig. 3(h). These observations are consistent with previous research, which showed that AR increases with higher V^* and lower H [64]. Similar to PDMS-based inks, the shape change of LM droplets in ExSil-based inks would be expected not to occur during extrusion through the nozzle as all the ExSil-based inks in this study have lower η_0 than the highest PDMS-based ink ($\phi = 50\,\%$, $\psi = 10\,\%$) viscosity (Fig. 2(d) and (g)). Additionally, ExSil-based inks exhibit increasing shear stress with increasing shear rate (Fig. S11(c)) and viscoelastic properties (Fig. S11(d)). Therefore, the shape changes of LM droplets within ExSil-based ink also occurs after extrusion from the nozzle. Owing to these similarities between PDMS- and ExSil-based inks and the higher range of achievable viscosity with PDMS (ExSil prepolymer is more viscous which limits the lower end of the range), we will only analyze PDMS-based inks in the following sections. However, ExSil-based inks are also presented in this study as the work time for both PDMS and ExSil prepolymers is strikingly different (24 h for ExSil and 4 h for PDMS) which allows for higher processing time for ExSil-based inks and could be advantageous for DIW 3D printed parts with multiple layers or for parts that involve an in-situ curing and/or imaging characterization step during the fabrication process.

2.4 Effect of ink parameters (η_0 and D) on LM droplet AR

Next, we investigated the effect of ink parameters (η_0 and D) on the AR of LM droplets in printed LM-polymer inks. The addition of FS to LM-polymer inks is desirable to increase the AR of LM droplets during printing (Fig. 3). However, as the content of FS is increased, the LM droplet is decreased resulting in smaller LM droplet AR [64]. To tailor the D of the LM droplets and η_0 of the ink, hexane was first added to the PDMS prepolymer matrix (including dispersed FS) to control the viscosity of the emulsion during ink formulation. Subsequently, LM was added and shear mixed to form the LM-polymer ink (see Material and Methods for details). The hexane was then removed prior to rheological analysis or printing.

Steady-state flow shear rate sweep tests were conducted to measure the rheological properties of each ink as a function of LM droplet size D. This sweep test data is shown in Fig. 4(a) and η_0 calculated from Carreau-Yasuda model fit in Fig. S12. We observed that the viscosity of the PDMS-based LM inks increase with FS loading and decreasing LM droplet D. Importantly, through the ink formulation process, the D of LM droplets can be controlled from 40 to 280 μm for inks with $\psi = 5\,\%$ and from 90 to 250 μm for inks with $\psi = 10\,\%$ by adding hexane during mixing process as measured through optical microscopy (Fig. 4(b)). As depicted in Fig. 4(c), for fixed printing conditions ($V^* = 12$ and $H = 40$ μm), the ink with higher η_0 and larger D results in higher LM droplet AR. The ability to create higher LM droplet AR is due to the higher shear stress experienced by the LM droplets. This results from the higher η_0 of the ink and the higher possibility of larger LM D to be elongated as the droplets are more compliant as the stiff surface oxide plays a smaller role in the deformation of larger droplets [76, 77].

The effect of D and η_0 on the AR of LM droplets in printed LM inks is shown in Fig. 4(d). First, when inks with similar low viscosity ($1.0\times10^3 < \eta_0 < 2.0\times10^3$ Pa·s) are printed, D has a critical effect on controlling the AR of LM droplets. For example, $\psi = 5\,\%$, $D =$

250 μm can achieve a high AR of 8.1 with the printing condition of $V^* = 12$, $H = 40\,\mu m$, compared to $\psi = 5\,\%$, $D = 90\ \mu m$ ($AR = 3.7$). Furthermore, even though the ink with larger D is printed at a higher nozzle height ($H = 300\ \mu m$), it still shows an AR of 5.2. This AR value is higher than the AR of $\psi = 5\,\%$, $D = 90\ \mu m$ ink printed at $V^* = 12$ and $H = 40\ \mu m$. Therefore, when the inks have η_0 in the order of 10^3 Pa·s, D plays a significant role in determining the AR of LM droplets.

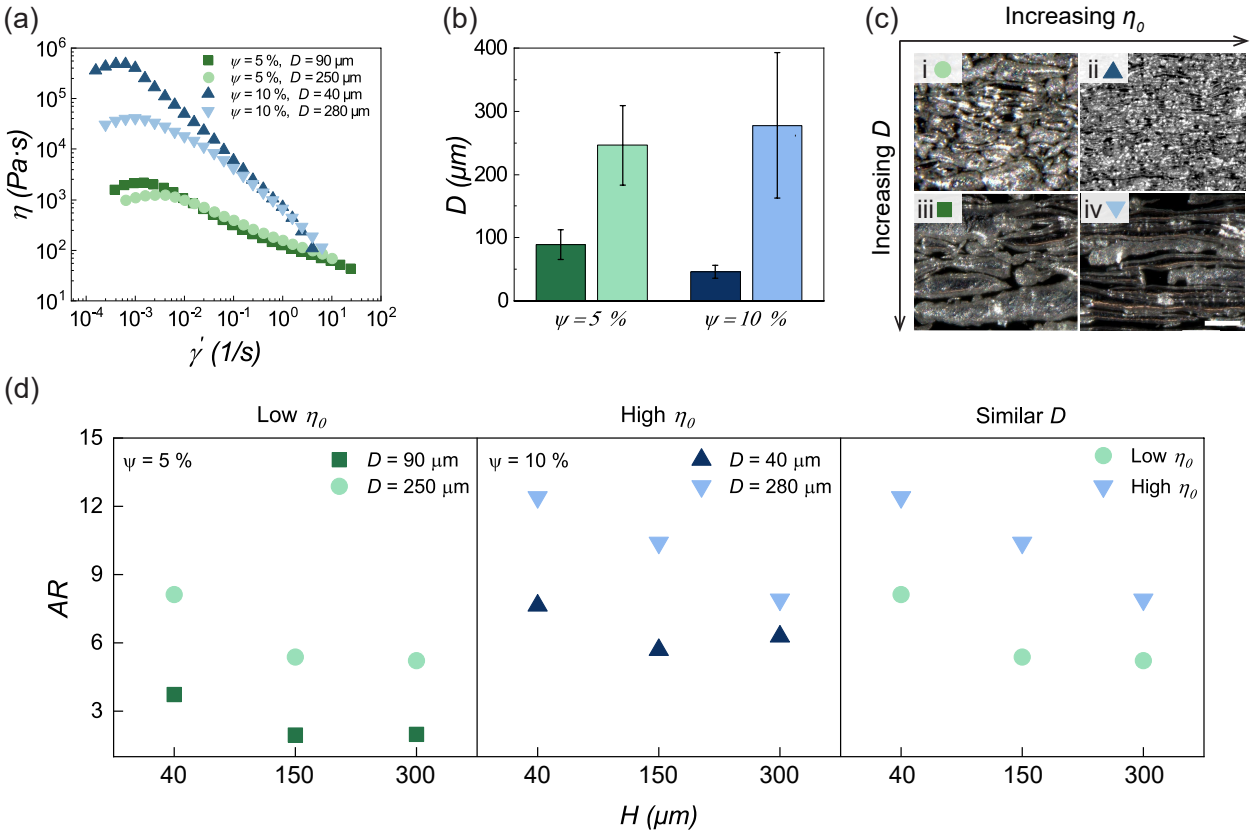

Fig. 4 Effect of η_0 and D on the AR of LMs in printed material. All PDMS-based inks in here include $\phi = 50\,\%$. (a) η vs. $\dot{\gamma}$ results with different FS contents ($\psi = 5$ *or* $10\,\%$) and D. (b) D of different inks. Error bars represent ± 1 standard deviation of Gaussian fits to the particle analysis histograms from micrograph image analysis. It follows legend in (a). (c) Microscope images of different PDMS-based LM inks with a fixed printing condition ($V^* = 12$, $H = 40\ \mu m$): i) $\psi = 5\,\%$, $D = 90\ \mu m$, ii) $\psi = 10\,\%$, $D = 40\ \mu m$, iii) $\psi = 5\,\%$, $D = 250\ \mu m$, iv) $\psi = 10\,\%$, $D = 280\ \mu m$. All images have the same scale bar of 100 μm. (d) The AR of LM droplets in printed PDMS-based inks with different print heights. (c-d) follow the legend in (a). The log-normal distributions of AR for $D = 250\ \mu m$ and $D = 280\ \mu m$ inks are presented in Fig. S13.

Secondly, the effect of D on AR in highly viscous inks ($\eta_0 > 3.7{\times}10^5$ Pa·s) is demonstrated

in the middle plot of Fig. 4(d). In this high viscosity regime, the maximum AR is dictated by D of LM droplets and shows a similar trend as in low η_0 regime. For example, the ink with larger D of 280 μm results in a higher AR (12.4) compared to the ink with D = 40 μm (AR = 7.6) when printed at same condition (V^* = 12 and H = 40 μm). It means that D is also a dominant factor that determines AR for LM inks that have a high η_0 ($> 3.7\times10^5$ Pa·s). Additionally, both of these inks still show higher AR (> 6.3) even when printed at higher nozzle height of H = 300 μm. So, when the inks are in high viscosity regime ($\eta_0 > 3.7\times10^5$), inks with a larger D show a higher AR than ink with a smaller D.

Thirdly, an ink with large D ($\geq$ 250 μm) and minimum threshold η_0 ($>$ 500 Pa·s) can result in elongated LM droplets ($AR > 5.0$) even with a higher print height (H = 300 μm). Additionally, PDMS, ϕ = 50 %, ψ = 10 %, D = 280 μm ink can achieve a higher LM droplet AR of 12.4 compared to ϕ = 50 %, ψ = 5 %, D = 250 μm ink (AR = 8.1), though they have similar D. Thus, when two inks have similar D and are printed with the same printing conditions, we can expect that ink with higher η_0 will result in a higher LM droplet AR.

To summarize, if an ink has a sufficiently large D ($\geq$ 250 μm) or a sufficiently high η_0 ($> 3.7\times10^5$ Pa·s), higher AR of LM droplets can be achieved with a printing condition of V^* = 12 and at all Hs in this study (40, 150, 300 μm) whereas at lower V^* (1 or 6), a high AR (> 5) of LM droplets cannot be achieved in any of the inks (Fig. S14).

2.5 The role of the Ga-oxide shell in LM droplet shape control

One of the distinct aspects of LM when compared to other liquid fillers is the thin Ga-oxide layer (0.7-3 nm) that spontaneously forms in the presence of ppm levels of oxygen on the surface of the LM droplets [78–80]. This oxide shell provides mechanical stability to the droplets and also acts as a surfactant when dispersed in polymers [81–83]. To demonstrate the important role of this oxide layer in LM droplet shape reconfiguration, we created two PDMS inks, one with glycerol (ϕ_{GC} = 50 %, ψ = 10 %,) and the other one with LM (ϕ_{LM} = 50 %, ψ = 5 %). We added different content of FS to the glycerol and LM inks to achieve a similar

droplet size and ensure $\eta_0 \geq 500$ Pa·s.

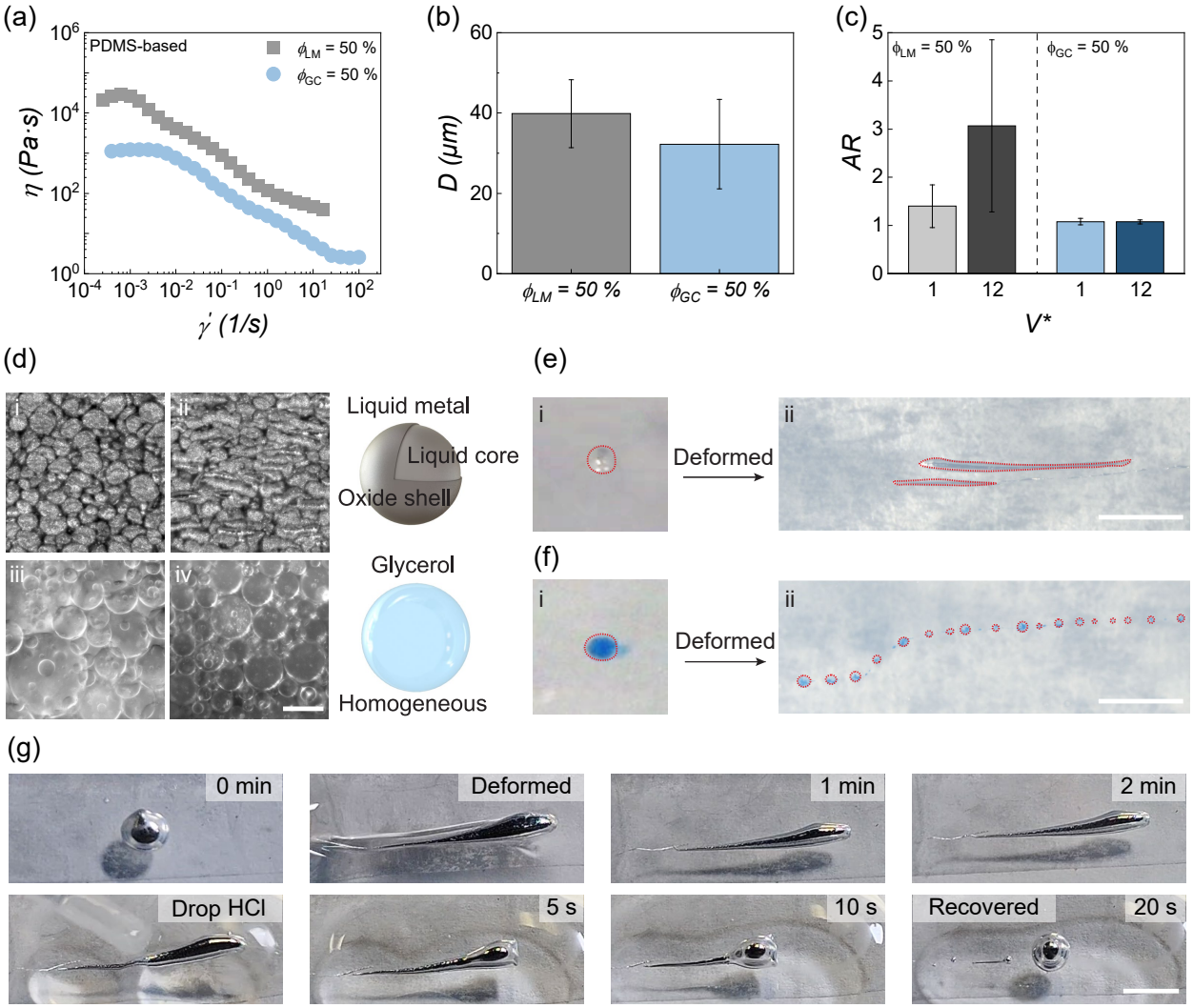

Fig. 5 Role of surface oxide layer in elongating LM droplets. (a) η vs. $\dot{\gamma}$ of PDMS, $\phi_{LM} = 50\,\%$, and $\phi_{GC} = 50\,\%$ ink. (b) D of two different inks. (c) AR of two different inks with different printing conditions, $V^* = 1$, 12 at $H = 40$ μm. (d) Microscope images of two different inks: PDMS, $\phi_{LM} = 50\,\%$, i) $V^* = 1$, ii) $V^* = 12$ with $H = 40$ μm and PDMS, $\phi_{GC} = 50\,\%$, iii) $V^* = 1$, iv) $V^* = 12$ with $H = 40$ μm. The scale bar is 40 μm. The schematic images show LM and glycerol droplet structures. Observation of droplets' shape change when they are deformed. i) Pristine state. ii) After deformed (5 min). (e) A LM droplet in PDMS, $\psi = 10\,\%$. (f) A glycerol droplet in PDMS, $\psi = 5\,\%$. The dashed red lines in (e) and (f) visually highlight the boundary of each droplet. The scale bar is 2 mm. (g) A LM droplet deformed in uncured PDMS with fumed silica ($\psi = 5\%$) followed by the addition of HCl on the surface. The scale bar is 500 μm. Error bars in (b) and (c) represent ± 1 standard deviation of Gaussian fits and log-normal fits, respectively, to the particle analysis histograms from micrograph image analysis.

Steady-state flow shear rate sweep tests were performed to characterize the rheological behavior (Fig. 5(a)). Even though the volume loading of the filler is the same for both inks and more FS is included in PDMS-glycerol ink ($\psi = 10\,\%$), the PDMS-LM ink has a higher viscosity. This is due to the presence of an oxide layer on LM in contrast to the fluid nature of glycerol droplet (see schematics in Fig. 5(d)). The thin oxide layer on the LM droplet surface, predominantly comprised of gallium oxide, strongly influences the interfacial rheological of the LM droplets [84]. Without the presence of this oxide layer, the rheological behavior of LM could be considered comparable to other liquid fillers such as glycerol. However, due to the oxide layer, the LM droplet has higher resistance to flow resulting in higher viscosity of LM inks compared to glycerol inks. The prepared inks were observed to have a similar D (Fig. 5(b)), which allows us to disregard the effect of D on the final AR when printed. These inks were printed with the same printing conditions, $V^* = 1$ or 12, and $H = 40$ μm. However, the resulting AR of each droplet was different as shown in Fig. 5(c) and (d). The LM droplets show an increase in AR from 1.4 to 3.1 as V^* is increased from 1 to 12, respectively, while the glycerol droplets have no observable change in AR as V^* is increased. We attribute this to two primary factors. First, the LM oxide layer is a solid state that leads high η_0. This results in a larger shear stress on the droplet during printing. Second, once the droplet is reconfigured into a high AR ellipsoid, the LM droplets rapidly reform the oxide layer to re-encapsulate and lock in the shape. The oxide layer forms even in the presence of ppm levels of oxygen [78]. In contrast, glycerol has no oxide shell and thus the surface tension drives a spherical droplet shape, and we do not observe a retained,stretched shape after removing the external force [85]. Therefore, we only observe that LM droplets elongate and maintain the deformed shape during the DIW printing process.

To qualitatively observe the shape change mechanism, a manual droplet deformation experiment with tweezers was conducted as shown in Fig. 5(e) and (f) with LM and glycerol droplets, respectively. Both droplets are $\sim$600 μm in size (Fig. S15). LM and glycerol droplets are placed in an uncured PDMS, $\psi = 5\,\%$ (Fig. 5(e-i)) and $\psi = 10\,\%$ mixture

(Fig. 5(f-i)), respectively, to mimic the DIW printing environment. The glycerol droplet is dyed with blue pigment to aid in visualization. As shown in Fig. 5(e-ii) and supplementary video 1, the LM droplet maintains its elongated shape after deforming, and does not split into small droplets. However, as shown in Fig. 5(f-ii) and supplementary movie S1, the glycerol droplet splits into several smaller droplets. For the larger LM and glycerol droplets ($D = 2$ mm), a shape recovery is observed after deforming the glycerol droplet (Fig. S16(a), supplementary movie S2) while LM droplet maintained its elongated shape after being deformed (Fig. S16(b), supplementary movie S2). Additionally, a LM droplet in a deformed state recovers its shape to spherical shape if the oxide layer is removed (supplementary movie S3). This is demonstrated in Fig. 5(g) where a LM droplet placed in an uncured PDMS, $\psi = 5\,\%$ is manually deformed by tweezers and maintains its elongated shape until the oxide layer is removed by exposing to hydrochloric acid (HCl) added on the PDMS surface. These experiments illustrate the unique and critical role of the Ga-oxide skin during DIW printing to lock in the programmed shape of the LM droplets.

2.6 Design maps for DIW of LM microstructures with desired AR

There are multiple printing process parameters and ink properties that can be utilized to control the AR of LM droplets in LM-polymer inks during DIW printing. To summarize our results and guide the design of LM microstructures during DIW printing, we created two quantitative design maps for droplet AR based on printing process parameters (V^* and H) and ink properties (η_0 and D). Fig. 6(a) describes the effect of the DIW printing process parameters (V^* and H) on the AR of LM droplets in PDMS-based inks ($\psi = 10\,\%$, $D = 280\ \mu m$). When the material parameters are fixed, the resultant AR of LM droplets as a function of printing conditions can be illustrated as three distinct regions in this design map. The regions in Fig. 6(a) are divided into three tiers based on the maximum achievable AR of LM droplets. For example, in Region 1, the $AR < 5$ at all levels of H. However, in Region 2, an $AR > 7$ can be achieved with all H conditions. Moreover, in Region 3, highly elongated

LM ($AR > 10$) is achievable by modifying the printing condition ($V^* > 10$ and $H < 150$ μm). Therefore, for DIW printing of LM ink, printing at higher V^* (12) and lower H (40 μm) will achieve the most elongated LM droplets.

Fig. 6(b) describes the overall effect of ink properties (η_0 and D) on the AR of LM droplets in PDMS-based inks for fixed printing conditions ($V^* = 12$, $H = 40$ μm). There are four different regions in this map with the gray regions representing the limitations of DIW processing (ink formulation and/or printing difficulties) of LM ($\phi = 50\,\%$) inks. In Region 1 of Fig. 6(b), an AR value greater than 5 cannot be achieved with LM inks. For example, although LM inks have a large D of about 300 μm, they do not have a sufficiently large η_0 to achieve printed LM droplets with high AR. Furthermore, even at high $\eta_0 \sim 10^4$ Pa·s, the small D of 50 μm prevents the printing of LM droplets with high AR values. In Region 2, LM inks can be printed with an AR greater than 6. If η_0 is smaller than 10^3 Pa·s, larger D is needed to achieve $AR > 6$. On the other hand, if the D is small ($< 100\mu m$), a higher η_0 is needed to achieve desired AR. In Region 3, the maximum AR (12.4) can be achieved. The LM inks that have $\eta_0 > 2.4 \times 10^4$ Pa·s, and $D > 150$ μm can print LM droplets with an $AR > 10$.

These maps present two primary approaches to increase the AR of LM droplets: 1) Modify printing conditions, 2) modify the rheological properties of the LM ink. If the material properties cannot be modified, a greater AR of LM droplets can be achieved through higher V^* and lower H. On the other hand, if printing condition cannot be changed, a higher AR can be achieved by increasing η_0 and D.

3 Conclusions

Through a DIW 3D printing strategy, we have determined the effects of the printing process parameters and ink properties on the LM droplet microstructure in LM-polymer inks during DIW printing, specifically the droplet AR. Tuning of LM droplet microstructure can

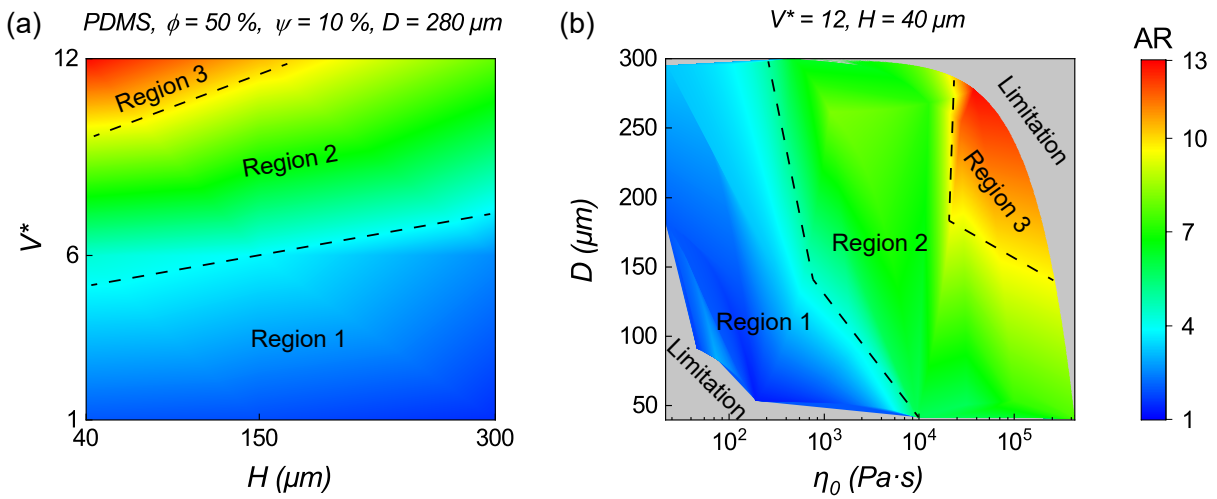

Fig. 6 Design maps for programming LM droplet AR through ink and processing parameters. (a) AR as a function of H and V^* for a high η_0 (3.7×10^4 Pa·s) and large D LM ink (PDMS, $\phi = 50\,\%$, $\psi = 10\,\%$, $D = 280\ \mu m$). (b) AR as a function of η_0 and D for inks with fixed processing conditions ($V^* = 12$ and $H = 40\ \mu m$). The gray region is not accessible for DIW printing of inks with $\phi = 50\,\%$ LM, and the color bar for AR is same for both maps.

be achieved by changing the printing parameters (V^*, H), and/or ink properties (η_0, D), resulting in LM droplets with shapes ranging from spherical ($AR = 1$) to ellipsoidal ($AR = 12.4$). To achieve LM droplets with high AR, LM-polymer inks should be formulated with high η_0 and large D and printed at high V^* and low H. The ink properties can be modified by adding FS and/or hexane during ink formulation. Adding more FS to the LM-polymer ink results in an increase in η_0 and a decrease in D at the same time. To increase D, hexane can be added during the mixing process and removed prior to printing. Additionally, the role of the oxide layer in LM droplet reconfiguration is demonstrated by comparing manually deformed LM and glycerol droplets in uncured PDMS elastomer. The LM oxide layer increases η_0 of the ink and forms a new oxide layer instantaneously after being deformed through the DIW printing process, enabling the retention of an elongated shape.

Finally, we provide two design maps, one for tuning printing parameters and another for tuning ink properties to achieve the desired AR of LM droplets in the printed material through the DIW process. These design maps rationally guide the DIW printing of LM-polymer inks for achieving spatially controlled LM architectures through programming the

rheological properties of LM inks or DIW printing conditions. This new capability provides a path towards achieving printed parts with spatially-tuned electrical, thermal, and mechanical properties. Additionally, such design maps could be created for other functional fillers such as multiphase solid-in-liquid magnetic filler emulsions with polymers and immiscible polymer mixtures to achieve spatially controlled microstructures and desired properties through DIW printing. Future work could also be focused on realizing such elongated microstructures in other fluid fillers by tuning the viscosity of the mixture and the architecture of the filler droplet to have a pseudo oxide-like layer either by incorporating surfactants or ligands that form the interface of the droplet and the polymer matrix. In summary, the combination of these two design maps offers valuable insights and opportunities for the additive manufacturing and liquid metal communities to create innovative materials and devices that possess unique multifunctional capabilities.

4 Material and Methods

4.1 Materials and ink fabrication

LM is a eutectic alloy of gallium and indium (EGaIn) that was prepared by mixing Ga:In (3:1 ratio by mass) and homogenized on a hot plate at 200 °C overnight. The LM emulsion inks were fabricated by homogeneously dispersing LM as droplets in either PDMS Sylgard 184 (Dow) or ExSil 100 (Gelest Inc.) by using a planetary centrifugal mixer (DAC 1200-500 VAC, FlackTek speed mixer). The mixing process was performed at specified speed and time profiles to achieve desired D of LM droplets in the ink. General PDMS- and ExSil-based inks were mixed at 800 rpm for 1 minute with the addition of LM ($\phi = 50\,\%$). Fumed silica (hydrophobic, Eastchem) was added at the same time with the addition of LM as a rheological modifier up to $\psi = 10\,\%$ of the elastomer matrix to increase the viscosity of the low viscous inks. For creating inks with larger D (250-280 μm) LM droplets, hexane was premixed with the uncured elastomer in a 1:10 ratio by weight for PDMS, $\psi = 5\,\%$ inks and

at a 3:10 ratio for PDMS, $\psi = 10\,\%$ inks before adding LM at $\phi = 50\,\%$ to both. Then, the inks were placed in a vacuum chamber for 3 h to remove any residual hexane before printing. The Glycerol emulsion inks were fabricated by mixing $\phi = 50\,\%$ glycerol (Acros Organics), in PDMS, $\psi = 10\,\%$ at 600 rpm for 1 minute. To match the D of LM to glycerol, $\phi = 50\,\%$ LM, $\psi = 5\,\%$ FS were mixed in PDMS at 2000 rpm for 5 minutes.

4.2 Material extrusion setup

The prepared inks were transferred to a 10 ml syringe (BD 10 mL Syringe) with a smooth flow nozzle that has a 0.84 mm inner diameter. The syringe was placed in a Hyrel SR 3D printer with an SDS-10 syringe head. Single-layer samples were printed on a PET film (McMaster-Carr) that has a thickness of 100 μm. An extrusion velocity of 4.1 mm s^{-1} was used for $V^* = 1$, 6, and 12. Print head velocity was 4.1, 24.6, and 49.2 mm s^{-1} for $V^* = 1$, 6, and 12, respectively. After printing, all samples were cured in a convection oven at 100 °C for a minimum of 2 h.

4.3 Optical microscopy

Images of the printed samples were obtained using a Zeiss Axiozoom v16 stereo-microscope, and image analysis was performed on the microscope images in Fiji software. LM droplets were outlined manually and converted into a binary image with elastomer and LM droplet areas. An ellipse fit was performed on each LM droplet area and major axis was considered as the droplet size D for spherical droplets. The ratio of the major to the minor axis of the ellipse was presented as the AR of the LM or glycerol droplet. A log-normal fit was applied on this data to analyze the AR distribution of printed LM droplets. A Gaussian distribution function was applied to analyze the distribution of D for spherical LM and glycerol droplets. The log-normal and Gaussian fits were performed in Origin software.

4.4 Rheological analysis

Rheological parameters of the inks were measured using an AR-G2 rotational rheometer (TA instruments). Two parallel plates with 25 mm in diameter and a 1 mm gap were used for all rheological analysis. The apparent viscosity was measured by flow sweep test with shear rates from 0.001 to 100 s^{-1}. The storage modulus and loss modulus were measured using a standard oscillatory amplitude sweep test, with an oscillation strain range from 0.01 to 100 % and an angular frequency of 1 Hz. All measurements were conducted at room temperature ($\sim$ 22 °C). The Carreau-Yasuda model was fit on the apparent viscosity data to obtain zero-shear viscosity in Origin software. The parameters related to the fitting were presented in Table S1.

4.5 LM and glycerol reconfiguration test

For rheology experiments, PDMS-based inks with $\phi = 50\,\%$ LM, $\psi = 5\,\%$ for LM droplets, and $\phi = 50\,\%$ glycerol, $\psi = 10\,\%$ for glycerol droplets were fabricated by using FlackTek mixer with mixing conditions of 2000 rpm and 5 min for LM inks and 600 rpm 1 min for glycerol inks. For the deformation experiments, glycerol was dyed with blue pigment (Smooth-On Silc Pig). LM and glycerol droplets were placed in an uncured PDMS elastomer with $\psi = 5\,\%$ for LM, $\psi = 10\,\%$ for glycerol by using a syringe with a metal tip (diameter: 0.4 mm). LM and glycerol droplets were manually deformed with tweezers. To demonstrate oxide layer's role in reconfiguration, hydrochloric acid (HCl, Fisher scientific) was used to remove oxide layer.

4.6 Design maps

To generate design maps, analyses of LM droplet AR from different inks and printing conditions were used. To make the design map in Fig. 6(a) for printing condition (V^* and H), 9 data points were used with a combination of V^* =1, 6, 12 and H = 40, 150, 300 μm. For a

design map of ink properties in Fig. 6(b), 15 data points were used. Data includes the range of 2×10^1 Pa·s $< \eta_0 < 5 \times 10^5$ Pa·s and 40 $\mu m < D <$ 300 μm. For creating the maps, the data points were first plotted as a 3D plot and then contour color fill function was utilized to generate the colored regions in Origin Pro data analysis software.

CRediT authorship contribution statement

Ohnyoung Hur: Writing - original draft, review & editing, designed research, performed experiments, and analyzed data. **Ravi Tutika:** Writing - original draft, review & editing, designed research, performed experiments, and analyzed data. **Neal Klemba:** Performed experiments. **Eric J. Markvicka:** Writing - original draft, review & editing, designed research, analyzed data, and funding acquisition. **Michael D. Bartlett:** Writing - original draft, review & editing, designed research, analyzed data, and funding acquisition.

Declaration of Competing Interest

The authors declare that they have no known competing financial interests or personal relationships that could have appeared to influence the work reported in this paper.

Acknowledgments

OH, RT, and MB acknowledge support through NSF (No. CMMI-2054409). NK acknowledges support from Brown University through a SPRINT LINK award for undergraduate internship. EM acknowledges support through the NSF (No. CMMI-2054411).

References

[1] Michael J Ford, Yunsik Ohm, Keene Chin, and Carmel Majidi. Composites of functional polymers: Toward physical intelligence using flexible and soft materials. *Journal of Materials Research*, pages 1–23, 2022.

[2] Metin Sitti. Physical intelligence as a new paradigm. *Extreme Mechanics Letters*, 46:101340, 2021.

[3] Aslan Miriyev and Mirko Kovač. Skills for physical artificial intelligence. *Nature Machine Intelligence*, 2(11):658–660, 2020.

[4] David Howard, Agoston E Eiben, Danielle Frances Kennedy, Jean-Baptiste Mouret, Philip Valencia, and Dave Winkler. Evolving embodied intelligence from materials to machines. *Nature Machine Intelligence*, 1(1):12–19, 2019.

[5] Kutay Sagdic, Ismail Eş, Metin Sitti, and Fatih Inci. Smart materials: rational design in biosystems via artificial intelligence. *Trends in Biotechnology*, 2022.

[6] Jordan R Raney, Brett G Compton, Jochen Mueller, Thomas J Ober, Kristina Shea, and Jennifer A Lewis. Rotational 3d printing of damage-tolerant composites with programmable mechanics. *Proceedings of the National Academy of Sciences*, 115(6):1198–1203, 2018.

[7] Dharneedar Ravichandran, Weiheng Xu, Sayli Jambhulkar, Yuxiang Zhu, Mounika Kakarla, Mohammed Bawareth, and Kenan Song. Intrinsic field-induced nanoparticle assembly in three-dimensional (3d) printing polymeric composites. *ACS Applied Materials & Interfaces*, 13(44):52274–52294, 2021.

[8] Jingjiang Wei, Hang Ping, Jingjing Xie, Zhaoyong Zou, Kun Wang, Hao Xie, Weimin Wang, Liwen Lei, and Zhengyi Fu. Bioprocess-inspired microscale additive manufac-

turing of multilayered tio2/polymer composites with enamel-like structures and high mechanical properties. *Advanced Functional Materials*, 30(4):1904880, 2020.

[9] Brandon Hayes, Travis Hainsworth, and Robert MacCurdy. Liquid–solid co-printing of multi-material 3d fluidic devices via material jetting. *Additive Manufacturing*, 55:102785, 2022.

[10] Shangqin Yuan, Shaoying Li, Jihong Zhu, and Yunlong Tang. Additive manufacturing of polymeric composites from material processing to structural design. *Composites Part B: Engineering*, 219:108903, 2021.

[11] Amir Asadi and Kyriaki Kalaitzidou. Process-structure-property relationship in polymer nanocomposites. In *Experimental characterization, predictive mechanical and thermal modeling of nanostructures and their polymer composites*, pages 25–100. Elsevier, 2018.

[12] Soyeon Park, Wan Shou, Liane Makatura, Wojciech Matusik, and Kun Kelvin Fu. 3d printing of polymer composites: Materials, processes, and applications. *Matter*, 5(1):43–76, 2022.

[13] Ye Wang, Ian M McAninch, Antoine P Delarue, Christopher J Hansen, E Jason Robinette, and Amy M Peterson. Additively manufactured thermosetting elastomer composites: small changes in resin formulation lead to large changes in mechanical and viscoelastic properties. *Materials Advances*, 4(2):607–615, 2023.

[14] Chuhong Zhang, Yijun Li, Wenbin Kang, Xingang Liu, and Qi Wang. Current advances and future perspectives of additive manufacturing for functional polymeric materials and devices. *SusMat*, 1(1):127–147, 2021.

[15] Jiayao Chen, Xiaojiang Liu, Yujia Tian, Wei Zhu, Chunze Yan, Yusheng Shi, Ling Bing Kong, Hang Jerry Qi, and Kun Zhou. 3d-printed anisotropic polymer materials for functional applications. *Advanced Materials*, 34(5):2102877, 2022.

[16] Carmel Majidi, Kaveh Alizadeh, Yunsik Ohm, Andre Silva, and Mahmoud Tavakoli. Liquid metal polymer composites: from printed stretchable circuits to soft actuators. *Flexible and Printed Electronics*, 7(1):013002, 2022.

[17] Youngshang Han, Leif-Erik Simonsen, and Mohammad H Malakooti. Printing liquid metal elastomer composites for high-performance stretchable thermoelectric generators. *Advanced Energy Materials*, 12(34):2201413, 2022.

[18] Yoon Young Choi, Dong Hae Ho, and Jeong Ho Cho. Self-healable hydrogel–liquid metal composite platform enabled by a 3d printed stamp for a multimodular sensor system. *ACS applied materials & interfaces*, 12(8):9824–9832, 2020.

[19] Mason Zadan, Cerwyn Chiew, Carmel Majidi, and Mohammad H Malakooti. Liquid metal architectures for soft and wearable energy harvesting devices. *Multifunctional Materials*, 4(1):012001, 2021.

[20] Priyanuj Bhuyan, Yuwen Wei, Dongkyun Cho, Umesh T Nakate, Seoyeon Kim, Sangmin Lee, Minjae Choe, Hongchan Jeon, and Sungjune Park. Multifunctional ultrastretchable and ultrasoft electronics enabled by uncrosslinked polysiloxane elastomers patterned with rheologically modified liquid metal electrodes: Beyond current soft and stretchable electronics. *Chemical Engineering Journal*, 453:139832, 2023.

[21] Oluwaseun A Alo, David Mauchline, and Iyiola O Otunniyi. 3d-printed functional polymers and nanocomposites: Defects characterization and product quality improvement. *Advanced Engineering Materials*, 24(5):2101219, 2022.

[22] MASR Saadi, Alianna Maguire, Neethu T Pottackal, Md Shajedul Hoque Thakur, Maruf Md Ikram, A John Hart, Pulickel M Ajayan, and Muhammad M Rahman. Direct ink writing: a 3d printing technology for diverse materials. *Advanced Materials*, 34(28):2108855, 2022.

[23] Sara Abdollahi, Eric J Markvicka, Carmel Majidi, and Adam W Feinberg. 3d printing silicone elastomer for patient-specific wearable pulse oximeter. *Advanced healthcare materials*, 9(15):1901735, 2020.

[24] Ruizhe Xing, Jiayi Yang, Dongguang Zhang, Wei Gong, Taylor V Neumann, Meixiang Wang, Renliang Huang, Jie Kong, Wei Qi, and Michael D Dickey. Metallic gels for conductive 3d and 4d printing. *Matter*, 6(7):2248–2262, 2023.

[25] Kalaimani Markandan and Chang Quan Lai. Fabrication, properties and applications of polymer composites additively manufactured with filler alignment control: A review. *Composites Part B: Engineering*, 256:110661, 2023.

[26] Yuan Sui, Caicong Li, Shiyu Feng, Yao Ling, Cong Li, Xiaosong Wu, Jinghui Shen, Jian Song, Hailong Peng, and Weiguo Huang. Patterning, morphing, and coding of gel composites by direct ink writing. *Journal of Materials Chemistry A*, 9(13):8586–8597, 2021.

[27] Ruihua Guan, Hengyu Zheng, Qingxiao Liu, KangTai Ou, Dian-sen Li, Jiang Fan, Qiang Fu, and Youyi Sun. Diw 3d printing of hybrid magnetorheological materials for application in soft robotic grippers. *Composites Science and Technology*, 223:109409, 2022.

[28] Arda Kotikian, Ryan L Truby, John William Boley, Timothy J White, and Jennifer A Lewis. 3d printing of liquid crystal elastomeric actuators with spatially programed nematic order. *Advanced materials*, 30(10):1706164, 2018.

[29] Stian K Romberg, Mohammad A Islam, Christopher J Hershey, Michael DeVinney, Chad E Duty, Vlastimil Kunc, and Brett G Compton. Linking thermoset ink rheology to the stability of 3d-printed structures. *Additive Manufacturing*, 37:101621, 2021.

[30] Arit Das, Eric L Gilmer, Saeid Biria, and Michael J Bortner. Importance of polymer rheology on material extrusion additive manufacturing: correlating process physics to print properties. *ACS Applied Polymer Materials*, 3(3):1218–1249, 2021.

[31] Osman Dogan Yirmibesoglu, Leif Erik Simonsen, Robert Manson, Joseph Davidson, Katherine Healy, Yigit Menguc, and Thomas Wallin. Multi-material direct ink writing of photocurable elastomeric foams. *Communications Materials*, 2(1):82, 2021.

[32] Philip J Scott, Daniel A Rau, Jianheng Wen, Mai Nguyen, Christopher R Kasprzak, Christopher B Williams, and Timothy E Long. Polymer-inorganic hybrid colloids for ultraviolet-assisted direct ink write of polymer nanocomposites. *Additive Manufacturing*, 35:101393, 2020.

[33] Daniel A Rau, Jackson S Bryant, John P Reynolds, Michael J Bortner, and Christopher B Williams. A dual-cure approach for the ultraviolet-assisted material extrusion of highly loaded opaque suspensions. *Additive Manufacturing*, 72:103616, 2023.

[34] Zhenyu Wang, Jun Ren, Rui Liu, Xinhu Sun, Dandan Huang, Wei Xu, Jing Jiang, Kaixue Ma, and Yu Liu. Three dimensional core-shell structured liquid metal/elastomer composite via coaxial direct ink writing for electromagnetic interference shielding. *Composites Part A: Applied Science and Manufacturing*, 136:105957, 2020.

[35] Taylor V Neumann, Emily G Facchine, Brian Leonardo, Saad Khan, and Michael D Dickey. Direct write printing of a self-encapsulating liquid metal–silicone composite. *Soft Matter*, 16(28):6608–6618, 2020.

[36] Cedric P Ambulo, Michael J Ford, Kyle Searles, Carmel Majidi, and Taylor H Ware. 4d-printable liquid metal–liquid crystal elastomer composites. *ACS applied materials & interfaces*, 13(11):12805–12813, 2020.

[37] Sumin Moon, Hanul Kim, Kyoungmun Lee, Jinwon Park, Yunho Kim, and Siyoung Q Choi. 3d printable concentrated liquid metal composite with high thermal conductivity. *Iscience*, 24(10):103183, 2021.

[38] Priyanuj Bhuyan, Yuwen Wei, Dongho Sin, Jaesang Yu, Changwoon Nah, Kwang-Un Jeong, Michael D Dickey, and Sungjune Park. Soft and stretchable liquid metal composites with shape memory and healable conductivity. *ACS Applied Materials & Interfaces*, 13(24):28916–28924, 2021.

[39] Wilson Kong, Zhongyong Wang, Nathan Casey, Mani M Korah, Aastha Uppal, Matthew D Green, Konrad Rykaczewski, and Robert Y Wang. High thermal conductivity in multiphase liquid metal and silicon carbide soft composites. *Advanced Materials Interfaces*, 8(14):2100069, 2021.

[40] Ravi Tutika, Shihuai H Zhou, Ralph E Napolitano, and Michael D Bartlett. Mechanical and functional tradeoffs in multiphase liquid metal, solid particle soft composites. *Advanced Functional Materials*, 28(45):1804336, 2018.

[41] Navid Kazem, Michael D Bartlett, and Carmel Majidi. Extreme toughening of soft materials with liquid metal. *Advanced Materials*, 30(22):1706594, 2018.

[42] Ethan J Krings, Haipeng Zhang, Suchit Sarin, Jeffery E Shield, Sangjin Ryu, and Eric J Markvicka. Lightweight, thermally conductive liquid metal elastomer composite with independently controllable thermal conductivity and density. *Small*, 17(52):2104762, 2021.

[43] Erin R Crater, Ravi Tutika, Robert B Moore, and Michael D Bartlett. X-ray scattering as an effective tool for characterizing liquid metal composite morphology. *Soft Matter*, 18(40):7762–7772, 2022.

[44] Sanhu Liu, Zhiwu Xu, Guoqiang Li, Zhengwei Li, Zihan Ye, Zirong Xu, Wenjun Chen, Dongdong Jin, and Xing Ma. Ultrasonic-enabled nondestructive and substrate-independent liquid metal ink sintering. *Advanced Science*, page 2301292, 2023.

[45] Yadong Xu, Yajuan Su, Xianchen Xu, Brian Arends, Ganggang Zhao, Daniel N Ackerman, Henry Huang, St Patrick Reid, Joshua L Santarpia, Chansong Kim, et al. Porous liquid metal–elastomer composites with high leakage resistance and antimicrobial property for skin-interfaced bioelectronics. *Science Advances*, 9(1):eadf0575, 2023.

[46] Shreyas Kanetkar, Najam Ul H Shah, Rohit M Gandhi, Aastha Uppal, Michael D Dickey, Robert Y Wang, and Konrad Rykaczewski. Fabrication of multiphase liquid metal composites containing gas and solid fillers: From pastes to foams. *ACS Applied Engineering Materials*, 2023.

[47] Michael D Bartlett, Navid Kazem, Matthew J Powell-Palm, Xiaonan Huang, Wenhuan Sun, Jonathan A Malen, and Carmel Majidi. High thermal conductivity in soft elastomers with elongated liquid metal inclusions. *Proceedings of the National Academy of Sciences*, 114(9):2143–2148, 2017.

[48] ABM Tahidul Haque, Ravi Tutika, Rachael L Byrum, and Michael D Bartlett. Programmable liquid metal microstructures for multifunctional soft thermal composites. *Advanced Functional Materials*, 30(25):2000832, 2020.

[49] Eric J Markvicka, Michael D Bartlett, Xiaonan Huang, and Carmel Majidi. An autonomously electrically self-healing liquid metal–elastomer composite for robust soft-matter robotics and electronics. *Nature materials*, 17(7):618–624, 2018.

[50] Ravi Tutika, ABM Tahidul Haque, and Michael D Bartlett. Self-healing liquid metal composite for reconfigurable and recyclable soft electronics. *Communications Materials*, 2(1):64, 2021.

[51] Zhijun Ma, Qiyao Huang, Qi Xu, Qiuna Zhuang, Xin Zhao, Yuhe Yang, Hua Qiu, Zhilu Yang, Cong Wang, Yang Chai, et al. Permeable superelastic liquid-metal fibre mat enables biocompatible and monolithic stretchable electronics. *Nature Materials*, 20(6):859–868, 2021.

[52] Carl J Thrasher, Zachary J Farrell, Nicholas J Morris, Carson L Willey, and Christopher E Tabor. Mechanoresponsive polymerized liquid metal networks. *Advanced Materials*, 31(40):1903864, 2019.

[53] Shanliangzi Liu, Dylan S Shah, and Rebecca Kramer-Bottiglio. Highly stretchable multilayer electronic circuits using biphasic gallium-indium. *Nature Materials*, 20(6):851–858, 2021.

[54] Mingkun Yang, Ying-xia Liu, Donglin Zhang, Chenrui Cao, Xiuchen Zhao, and Yongjun Huo. Size-controlled low-melting-point-alloy particle-incorporated transient liquid-phase epoxy composite conductive adhesive with high performances. *ACS Applied Polymer Materials*, 5(4):2760–2773, 2023.

[55] ABM Tahidul Haque, Dong Hae Ho, Dohgyu Hwang, Ravi Tutika, Chanhong Lee, and Michael D Bartlett. Electrically conductive liquid metal composite adhesives for reversible bonding of soft electronics. *Advanced Functional Materials*, page 2304101, 2023.

[56] Tyler A Pozarycki, Dohgyu Hwang, Edward J Barron III, Brittan T Wilcox, Ravi Tutika, and Michael D Bartlett. Tough bonding of liquid metal-elastomer composites for multifunctional adhesives. *Small*, 18(41):2203700, 2022.

[57] Shib Shankar Banerjee, Subhradeep Mandal, Injamamul Arief, Rama Kanta Layek, Anik Kumar Ghosh, Ke Yang, Jayant Kumar, Petr Formanek, Andreas Fery, Gert Heinrich, et al. Designing supertough and ultrastretchable liquid metal-embedded nat-

ural rubber composites for soft-matter engineering. *ACS Applied Materials & Interfaces*, 13(13):15610–15620, 2021.

[58] Yi Zheng, Zhizhu He, Yunxia Gao, and Jing Liu. Direct desktop printed-circuits-on-paper flexible electronics. *Scientific reports*, 3(1):1786, 2013.

[59] Hao Chang, Rui Guo, Ziqiao Sun, Hongzhang Wang, Yi Hou, Qian Wang, Wei Rao, and Jing Liu. Direct writing and repairable paper flexible electronics using nickel–liquid metal ink. *Advanced Materials Interfaces*, 5(20):1800571, 2018.

[60] Lei Wang and Jing Liu. Compatible hybrid 3d printing of metal and nonmetal inks for direct manufacture of end functional devices. *Science China Technological Sciences*, 57:2089–2095, 2014.

[61] Fanghang Deng, Quang-Kha Nguyen, and Pu Zhang. Multifunctional liquid metal lattice materials through hybrid design and manufacturing. *Additive Manufacturing*, 33:101117, 2020.

[62] Shengfu Mei, Yunxia Gao, Zhongshan Deng, and Jing Liu. Thermally conductive and highly electrically resistive grease through homogeneously dispersing liquid metal droplets inside methyl silicone oil. *Journal of Electronic Packaging*, 136(1):011009, 2014.

[63] Sen Chen, Hong-Zhang Wang, Rui-Qi Zhao, Wei Rao, and Jing Liu. Liquid metal composites. *Matter*, 2(6):1446–1480, 2020.

[64] Aaron Haake, Ravi Tutika, Gwyneth M Schloer, Michael D Bartlett, and Eric J Markvicka. On-demand programming of liquid metal-composite microstructures through direct ink write 3d printing. *Advanced Materials*, 34(20):2200182, 2022.

[65] Tingting Ma, Ruiquan Yang, Zhong Zheng, and Yihu Song. Rheology of fumed silica/polydimethylsiloxane suspensions. *Journal of Rheology*, 61(2):205–215, 2017.

[66] Jean-Noël Paquien, Jocelyne Galy, Jean-François Gérard, and Alain Pouchelon. Rheological studies of fumed silica–polydimethylsiloxane suspensions. *Colloids and Surfaces A: Physicochemical and Engineering Aspects*, 260(1-3):165–172, 2005.

[67] Pierre J Carreau. Rheological equations from molecular network theories. *Transactions of the Society of Rheology*, 16(1):99–127, 1972.

[68] Montgomery T. Shaw. On estimating the zero-shear-rate viscosity: Tests with PIB and PDMS. *AIP Conference Proceedings*, 1779(1):070011, 10 2016.

[69] Ruchira Tandel and B Arda Gozen. Direct-ink-writing of liquid metal-graphene-based polymer composites: Composition-processing-property relationships. *Journal of Materials Processing Technology*, 302:117470, 2022.

[70] Lisa Biasetto, Andy Gleadall, and Vanessa Gastaldi. Ink tuning for direct ink writing of planar metallic lattices. *Advanced Engineering Materials*, 2023.

[71] James P Lewicki, Jennifer N Rodriguez, Cheng Zhu, Marcus A Worsley, Amanda S Wu, Yuliya Kanarska, John D Horn, Eric B Duoss, Jason M Ortega, William Elmer, et al. 3d-printing of meso-structurally ordered carbon fiber/polymer composites with unprecedented orthotropic physical properties. *Scientific reports*, 7(1):43401, 2017.

[72] Amanda Koh, Jennifer Sietins, Geoffrey Slipher, and Randy Mrozek. Deformable liquid metal polymer composites with tunable electronic and mechanical properties. *Journal of Materials Research*, 33(17):2443–2453, 2018.

[73] Cheng Qian and David Julian McClements. Formation of nanoemulsions stabilized by model food-grade emulsifiers using high-pressure homogenization: Factors affecting particle size. *Food hydrocolloids*, 25(5):1000–1008, 2011.

[74] Gaabhin Ryu, Inkyu Park, and Hyoungsoo Kim. Liquid metal micro-and nanodroplets: Characteristics, fabrication techniques, and applications. *ACS omega*, 8(18):15819–15830, 2023.

[75] Wilson Kong, Zhongyong Wang, Meng Wang, Kenneth C Manning, Aastha Uppal, Matthew D Green, Robert Y Wang, and Konrad Rykaczewski. Oxide-mediated formation of chemically stable tungsten–liquid metal mixtures for enhanced thermal interfaces. *Advanced Materials*, 31(44):1904309, 2019.

[76] Trevor R Lear, Seok-Hee Hyun, John William Boley, Edward L White, David H Thompson, and Rebecca K Kramer. Liquid metal particle popping: Macroscale to nanoscale. *Extreme Mechanics Letters*, 13:126–134, 2017.

[77] Mohammed G Mohammed and Rebecca Kramer. All-printed flexible and stretchable electronics. *Advanced Materials*, 29(19):1604965, 2017.

[78] Eric S Elton, Thomas C Reeve, Luke E Thornley, Ishan D Joshipura, Phillip H Paul, Andrew J Pascall, and Jason R Jeffries. Dramatic effect of oxide on measured liquid metal rheology. *Journal of Rheology*, 64(1):119–128, 2020.

[79] Yiliang Lin, Christopher Cooper, Meng Wang, Jacob J Adams, Jan Genzer, and Michael D Dickey. Handwritten, soft circuit boards and antennas using liquid metal nanoparticles. *Small*, 11(48):6397–6403, 2015.

[80] MJ Regan, H Tostmann, Peter S Pershan, OM Magnussen, E DiMasi, BM Ocko, and M Deutsch. X-ray study of the oxidation of liquid-gallium surfaces. *Physical Review B*, 55(16):10786, 1997.

[81] Collin Ladd, Ju-Hee So, John Muth, and Michael D Dickey. 3d printing of free standing liquid metal microstructures. *Advanced Materials*, 25(36):5081–5085, 2013.

[82] Tanya Hutter, Wolfgang-Andreas C Bauer, Stephen R Elliott, and Wilhelm TS Huck. Formation of spherical and non-spherical eutectic gallium-indium liquid-metal microdroplets in microfluidic channels at room temperature. *Advanced Functional Materials*, 22(12):2624–2631, 2012.

[83] Yiliang Lin, Jan Genzer, and Michael D Dickey. Attributes, fabrication, and applications of gallium-based liquid metal particles. *Advanced Science*, 7(12):2000192, 2020.

[84] Alan R Jacob, Dishit P Parekh, Michael D Dickey, and Lilian C Hsiao. Interfacial rheology of gallium-based liquid metals. *Langmuir*, 35(36):11774–11783, 2019.

[85] P Mazurek, S Hvilsted, and AL Skov. Green silicone elastomer obtained from a counterintuitively stable mixture of glycerol and pdms. *Polymer*, 87:1–7, 2016.